Mon. Not. R. Astron. Soc. **000**, 1–?? (2002) Printed 2 August 2013 (MN LATEX style file v2.2)

Chemical abundances in Orion protoplanetary discs: integral field spectroscopy of 180-331∗

Accepted ... Received ...

ABSTRACT

In the fourth in a series of papers on Orion protoplanetary discs (proplyds) we present a spectroscopic analysis of proplyd 180-331, based on integral field observations with the Very Large Telescope/FLAMES fibre array with $0.31'' \times 0.31''$ spatial pixels. The proplyd and its vicinity are imaged in a variety of emission lines across a $6.8'' \times 4.3''$ area.

Key words: ISM – abundances; HII regions; ISM: individual objects – (180-331, Orion Nebula); stars: pre-main-sequence; protostars; planets and satellites: protoplanetary discs

1 INTRODUCTION

180-331 is a proplyd located southeast of the Trapezium cluster in the Orion nebula. It is of similar appearance to the prototype of the class, LV 2 (Laques & Vidal 1979), though it is several times fainter. The proplyd is accompanied by a stand-off bow shock on the side facing the Trapezium and it has a stubby tail pointing away from the source of incoming ionizing photons, θ^1 Ori C (Fig. 1). It is the third target in an observing programme which also included LV 2 (Tsamis et al. 2011; Tsamis & Walsh 2011) and HST 10 (Tsamis et al. 2013).

The aim of the programme was to perform the first study of element abundances in a representative sample of proplyds and to compare those with the abundances in the host M42 nebula and the Orion stellar association. By means of optical integral-field unit (IFU) spectroscopy with VLT FLAMES/Argus the local Orion nebula emission was subtracted and intrinsic spectra of the proplyds were obtained for physical and chemical analysis. In all cases the abundances were obtained following direct measurements of the electron temperature and density from suitable emission line ratios. A similar study was undertaken for the HST 1 proplyd by Mesa-Delgado et al. (2012) using the Calar Alto PMAS integral-field spectrograph. For HST 1 and HST 10 dynamic photoevaporation models of the sources were also constructed based on the Cloudy plasma code. The models provided very useful insights into the ionization structure, mass-loss rates, and expected lifetimes of the sources. They further helped to put the empirical physicochemical analyses on firm ground, leading to a better understanding of the uncertainties involved in the determination of abundances.

The current paper presents an analysis of 180-331 (hereafter called P3) based on the same techniques and provides an overview of the state-of-the-art in the field thus far. The paper is organized as follows. A description of the source and its Orion vicinity is given in Section 2. The VLT dataset specifications and reduction steps are outlined in Section 3. The analysis and results are presented in Section 4, followed by our conclusions in Section 5.

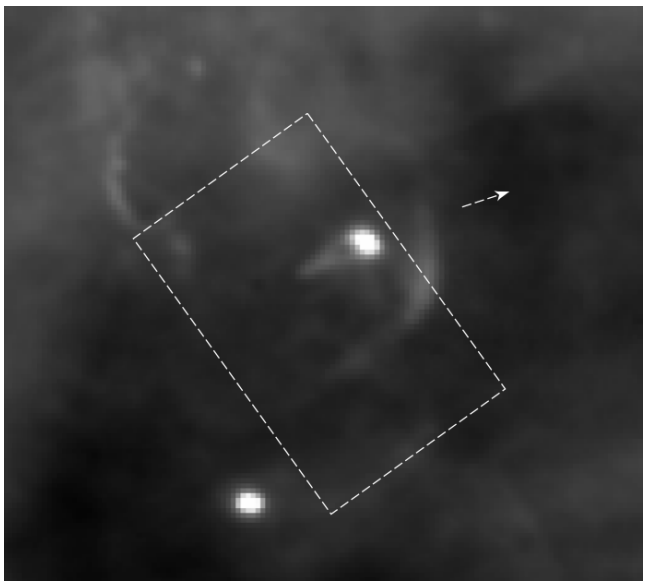

Figure 1. The object near the centre of this *HST* F656N (Hα + [N II]) image of the Orion nebula is the proplyd 180-331 at a scale of 0.0996 arcsec per pixel. Note the bow shock in front of the bright cusp. The dashed box is the $6.8'' \times 4.3''$ field of view of the VLT Argus IFU used in our observations. The arrow points towards θ^1 Ori C which lies 25 arcsec away from the cusp of the proplyd. North is up and east is to the left-hand side.

2 OBSERVATIONS AND DATA REDUCTION

Integral field spectroscopy of P3 was performed on the 8.2-m VLT/UT2 Kueyen at the ESO observatory on Paranal during 2007

∗ Based on observations made with ESO telescopes at the Paranal Observatory under programme 078.C-0247(A).

January and February with the fibre-fed FLAMES Giraffe spectrograph (Pasquini et al. 2002) and the Argus microlens array in high magnification mode. The cusp of the proplyd is centred at α_{J2000} = $5^h\ 35^m\ 18.032^s$, $\delta_{J2000} = -5^\circ\ 23'\ 30.59''$. A field of view of $6.8'' \times 4.3''$ was observed and 297 positional spectra were recorded in the optical range (3620–7184 Å) using a 2K × 4K CCD (with pixels of 15μm size). Six low resolution (LR) and one high resolution (HR) grating settings were employed (Table 1). The size of the angular resolution element was $0.31'' \times 0.31''$, corresponding to a spatial scale of 127×127 AU^2 at the distance to M42 (410 pc; Reid et al 2009). The measured seeing during the observations with the various gratings was typically 0.6–1.0″ FWHM and the observed airmasses were in the 1.1–2.1 range.

The cusp of the proplyd is observed near the western edge of the Argus IFU (Fig. 1). This is in common with the observations of the LV 2 and HST 10 proplyds from the same programme, and is due to a pointing error caused by the slight misalignment of the fiducial/guide fibres used for the acquisition of the target field. The observations are not detrimentally affected however, as in all cases the cusps of the proplyds are fully within the Argus field of view at the wavelengths of interest to our study.

The 2D data arrays were cosmic ray cleaned, flat fielded, wavelength calibrated, and extracted utilizing the girBLDRS pipeline developed by the Geneva Observatory as in Tsamis et al. (2013). The flux calibration was done within IRAF using contemporaneous exposures of various spectrophotometric standards for the grating settings: EG 21 (LR1), Feige 110 (LR2, LR3), LTT 7987 (LR4, 5, 6). The reduction products consisting of separate signal and error arrays were converted into (X, Y, λ) data cubes using IRAF routines and the Argus fibre positioning table.

The LR1 and LR2 data cubes were corrected for the effects of differential atmospheric refraction (DAR) using the algorithm of Walsh and Roy (1990) as in Tsamis et al. (2011). This was not necessary for the remaining datasets that were observed under low airmasses (<1.3). In a map of the [O III] λ4363 line from grating LR2 the cusp of the proplyd is observed at the very edge of the IFU and the observation is deemed unusable. A higher spectral resolution observation of the line from grating HR4 was adopted in its place. Residual spatial discrepancies were observed between the LR1,2,3 versus the LR4,5,6 and HR4 cubes; these were not caused by DAR but reflect the pointing accuracy of Argus with the particular fibre acquisition set-up. These were corrected for by shifting the LR4, 5, 6 spatial grid by one spaxel along both the long and short IFU axes, and the HR4 grid by four and one spaxels respectively, matching the peaks in emission of bright H I Balmer lines. The necessary rebinning has caused the blank columns on the edges of some of the maps discussed in Section 3.1.

Regarding the flux level of the extracted spectra, those taken with the LR5 and LR6 gratings were scaled by a factor of 0.793 via the flux of the [N II] λ5755 line (which falls on both LR4 and LR5 gratings) in order to match the bluer spectral coverage. The LR1 spectrum was scaled to that from LR2 using the H I λ3970 line common to both gratings. The LR2, LR3 and HR4 spectra were left unscaled: the relative uncertainty on the [O III] λ4363/Hγ ratio between the LR2 and HR4 gratings is ≃3 per cent.

Emission lines of interest from the various grating set-ups were fitted with Gaussian profiles in all ∼300 individual positional spectra. An automated procedure was used based on MIDAS tasks utilizing the Newton-Raphson least-squares method. The local continuum bracketing each line was fitted using a first order polynomial or a cubic spline. The resulting arrays were further processed within MIDAS and IRAF to form maps of the lines or continua and their signal-to-noise (S/N) ratios.

3 MAPPING THE PHYSICAL DIAGNOSTICS

3.1 Emission line maps and extracted spectra

The proplyd's cusp has an elliptical shape with a major axis of $\lesssim 0.6''$ as measured on the *HST* image of Fig. 1. It is therefore not resolved by the $0.31''\times0.31''$ Argus spaxels. Convolving the *HST* image with a Gaussian kernel whose FWHM matches the typical seeing disc during the observations results in a rebinned cusp area of ∼9 spaxels. This closely corresponds to the appearance of the cusp in the IFU line maps: in Fig. 2 a sample of these maps is shown, along with the degraded *HST* image for comparison. The Argus maps represent the continuum-subtracted line fluxes measured via Gaussian fitting as discussed above. The image quality is good and the proplyd's tail in visible in the [S II] λ4069 and λ6731 lines. The stand-off shock is ∼3 times fainter than the cusp, but it is rather blurred out at our effective resolution. The brightness contrast between the cusp and the shock is higher for the auroral collisional lines (CLs) (e.g. [N II] λ5755, [S II] λ4069) than for the nebular CLs or the H I lines. This most likely reflects the fact that the shock is of much lower density than the cusp.

Our analysis of the physical conditions in the proplyd relies on the extraction of its intrinsic background-subtracted spectrum. Given the small size of the proplyd we designate 9 spaxels – (X, Y) = (2–4, 12–14)[1] – as cusp. This minimizes potential contamination from the stand-off shock and from the Orion nebula following the background subtraction. The same number of spaxels was adopted in our Argus study of LV 2 which has a similarly sized cusp and was observed under ∼0.8″ seeing (Tsamis et al. 2011). We adopt as nebula background the mean spectrum of 24 spaxels clear from proplyd emission. The intrinsic cusp spectrum is then obtained by direct subtraction of the mean nebula spectrum from the proplyd cusp spectrum. This is the simplest procedure used in studies thus far and is equivalent to the proplyd being totally transparent or deeply embedded within the nebula, neglecting the fact that the cusp may be partially opaque to the emission of the gas column behind it (Vasconcelos et al. 2005; Tsamis et al. 2011; Mesa-Delgado et al. 2012).

3.2 Reddening

The interstellar reddening in the line of sight towards P3 was determined from a comparison of the observed Hα/Hβ, Hδ/Hβ, H I λ3970/Hβ ratios with their predicted Case B recombination theory ratios from Storey & Hummer (1995). We used the modification by Blagrave et al. (2007) of the reddening law of Cardelli, Clayton & Mathis (1989) with a total to selective extinction ratio $R_V = 5.5$ applicable to M42. The individual line ratios over the proplyd's cusp result in these mutually consistent c(Hβ) values: 0.84 ± 0.17 (Hα/Hβ), 0.64 ± 0.25 (Hδ/Hβ) and 0.86 ± 0.21 (H I λ3970/Hβ); these are mean values over the 9 spaxels of our designated cusp area. Our reddening determination is in good agreement with measurements obtained from *HST* image analysis by O'Dell (1998), and by O'Dell & Yusef-Zadeh (2000) who calculated c(Hβ) from the 20 cm/Hα ratio with a resolution of 1.7 arcsec. The latter study

[1] (X, Y) are respectively the short and long axes of the 14×22 spaxel array.

Table 1. Journal of VLT FLAMES/Argus observations.

Date (UT)	λ-range (Å)	Grating	$\lambda/\delta\lambda$	Exp. time (s)	Airmass	FWHM seeing arcsec
2007/01/29	3620–4081	LR1	12 800	4×150	1.7–1.9	0.7–0.9
2007/01/29	3964–4567	LR2	10 200	3×390	1.9–2.1	0.7
2007/02/06	4501–5078	LR3	12 000	4×206	1.1	0.9–1.0
2007/01/29	5015–5831	LR4	9 600	3×255	1.15	0.8–0.9
2007/01/29	5741–6524	LR5	11 800	3×255	1.2	0.7–0.8
2007/01/29	6438–7184	LR6	13 700	4×180	1.2–1.3	0.7
2007/01/28	4182–4392	HR4	32 500	4×292	1.2–1.3	0.6–0.7

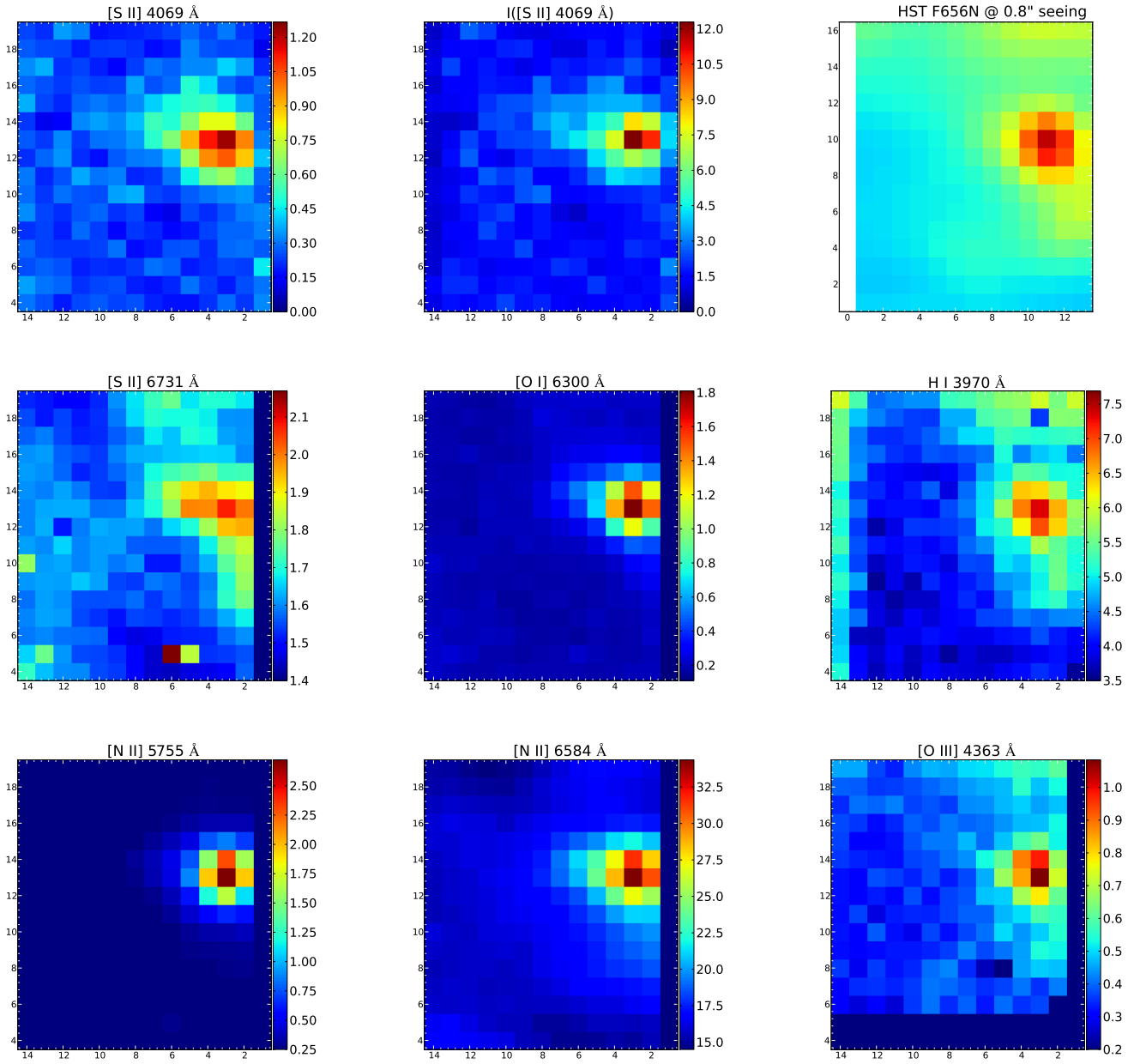

Figure 2. Emission line maps in units of 10^{-15} erg s^{-1} cm^{-2} spaxel^{-1}. I([S II]) is an example dereddened map. For comparison, the *HST* image of Fig. 1 is shown after convolution with a 0.8 arcsec FWHM Gaussian kernel and rebinned to the Argus spaxel size (colourscale in counts). For display purposes the field of view has been reduced to 5.27×4.20 arcsec^2. The spaxels subtend 0.31×0.31 arcsec^2. Masked outer columns are artefacts at the edges of the array introduced by the rebinning used to correct for the spatial shifts between individual gratings (see the text for details).

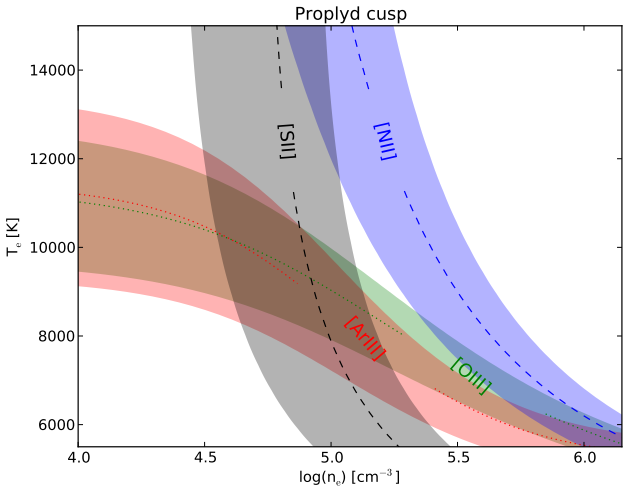

Figure 3. Diagnostic diagram applicable to mean line ratio values (dashed lines) over the cusp of P3 (9 spaxels): (X, Y) = (13–15, 2–4) in Argus array coordinates, where X, Y are respectively the long and short axes with a point of origin at the bottom right corner of the Argus IFU. The shaded areas denote the 1σ range of the corresponding ratios.

shows values of 0.6–0.8 across an area coincident with the Argus field of view.

The derived $c(\mathrm{H}\beta)$ map was used to convert the observed line maps to dereddened intensity maps relative to $I(\mathrm{H}\beta)$, such that $I(\lambda)/I(\mathrm{H}\beta) = F(\lambda)/F(\mathrm{H}\beta) \times 10^{c(\mathrm{H}\beta)f(\lambda)}$, where $f(\lambda)$ is the Blagrave et al. (2007) reddening curve. The dereddened intensity ratio maps were used for the subsequent physical analysis of the P3 field.

3.3 Electron density and temperature

The quoted uncertainties in Table 2 are associated with the measured variation of a given quantity across the sampled spaxels (the rms deviation from the mean). The formal uncertainties, propagated using the reduction pipeline-generated error arrays, on the density or temperature sensitive line ratios that are important for the abundance determinations are much smaller (less than two per cent).

Table 2. Dereddened line fluxes from the (background-subtracted) cusp of HST 10 and the local M42 background (in units such that Hβ = 100).

Line	HST 10 $I(\lambda)$	M42 $I(\lambda)$
c(Hβ)	0.81 ± 0.11	0.77 ± 0.03
[O II] λ3726	0.034 ± 0.019	63.9 ± 4.3
[O II] λ3729	0.019 ± 0.011	37.1 ± 3.1
[Ne III] λ3967	7.54 ± 2.51	6.00 ± 0.53
H I λ3970	14.6 ± 1.9	16.5 ± 0.58
[S II] λ4069	3.99 ± 1.71	1.00 ± 0.23
Hδ λ4101	25.8± 3.4	28.5 ±0.57
C II λ4267	0.164 ± 0.130	0.315± 0.076
Hγ λ4340	54.8 ± 15.4	55.4 ±0.85
[O III] λ4363	2.26 ± 0.83	1.35 ±0.13
He I λ4471	X ± 0.72	X ± 0.09
O II λ4649	0.140 ± 0.08	0.196 ± 0.039
[Fe III] λ4658	0.184 ± 0.092	0.447 ±0.055
[Ar IV] λ4711	–	X ± 0.030
[Ar IV] λ4740	–	X ± 0.033
Hβ λ4861	100.0	100.0
[O III] λ4959	83.6 ± 11.3	121.6 ±1.7
[Ar III] λ5192	0.166 ± 0.066	0.038 ± 0.044
[N I] λ5200	0.114 ± 0.084	0.163 ± 0.049
[Cl III] λ5518	0.113 ± 0.047	0.447 ± 0.025
[Cl III] λ5538	0.288 ± 0.053	0.629 ± 0.027
[O I] λ5577	0.143± 0.073	0.221 ± 0.017
[N II] λ5755	5.40 ± 1.65	0.560 ± 0.035
He I λ5876	14.8 ± 3.0	15.6 ± 0.32
[O I] λ6300	3.26 ± 0.89	0.413 ± 0.035
[S III] λ6312	1.92 ± 0.14	1.83 ± 0.05
Hα λ6563	272.0 ± 32.0	307.2 ± 6.2
C II λ6578	0.266 ± 0.106	0.404 ± 0.044
[N II] λ6584	34.7 ± 7.0	35.1 ± 1.1
[S II] λ6716	0.535 ± 0.266	2.27 ± 0.12
[S II] λ6731	1.10 ± 0.30	3.35 ± 0.14
[Ar III] λ7136	16.2 ± 2.6	13.1 ± 0.3
Hβ λ4861[a]	1642 ± 38	4385 ± 3
T_e([O III]) (K)	9300^{+1000}_{-1250}	8650 ± 200
T_e([N II]) (K)	–	10300^{+550}_{-700}
logN_e([S II]) (cm^{-3})	$4.92^{+0.21}_{-0.35}$	$3.53^{+0.19}_{-0.32}$
logN_e([S II]) (cm^{-3})	$\gtrsim$4.0	3.41 ± 0.10
logN_e([Cl III]) (cm^{-3})	$\gtrsim$4.0	3.12 ± 0.06
logN_e([O II]) (cm^{-3})	$\gtrsim$4.0	3.19 ± 0.11

[a] In units of 10^{-15} erg s^{-1} cm^{-2}. The cusp area comprises 9 spaxels and the background area 24 spaxels.